Check for updates

Vertically oriented SnS₂ on MoS₂ nanosheets for high-photoresponsivity and fast-response self-powered photoelectrochemical photodetectors

Yuqi Liu,† Chunhui Lu,† Mingwei Luo, Taotao Han, Yanqing Ge, Wen Dong,
Xinyi Xue, Yixuan Zhou [ID] * and Xinlong Xu [ID] *

Van der Waals heterostructures have great potential for the emerging self-powered photoelectrochemical photodetectors due to their outstanding photoelectric conversion capability and efficient interfacial carrier transportation. By considering the band alignment, structural design, and growth optimization, the heterostructures of vertically oriented SnS₂ with different densities on MoS₂ nanosheets are designed and fabricated using a two-step epitaxial growth method. Compared with SnS₂, MoS₂, and low density–vertical SnS₂/MoS₂ heterostructure, the high density–vertical SnS₂/MoS₂ heterostructure exhibits largely enhanced self-powered photodetection performances, such as a giant photocurrent density ($\sim$932.8 μA cm^{-2}), an excellent photoresponsivity (4.66 mA W^{-1}), and an ultrafast response/recovery time (3.6/6.4 ms) in the ultraviolet-visible range. This impressive enhancement of high density–vertical SnS₂/MoS₂ photodetectors is mainly ascribed to the essentially improved charge transfer and carrier transport of type-II band alignment heterostructures and the efficient light absorption from the unique light-trapping structure. In addition, the photoelectrocatalytic water splitting performance of the high density–vertical SnS₂/MoS₂ heterostructure also benefits from the type-II band alignment and the light-trapping structure. This work provides valuable inspiration for the design of two-dimensional optoelectronic and photoelectrochemical devices with improved performance by the morphology and heterostructure design.

New concepts

By considering the band alignment, structural design, and growth optimization, this study proposed a self-powered photoelectrochemical photodetector based on the SnS₂/MoS₂ heterostructure with trap-like vertically oriented nanostructures. To the best of our knowledge, this is the first report in which different morphologies of SnS₂/MoS₂ by a chemical vapor deposition method and a self-powered photoelectrochemical photodetector based on SnS₂/MoS₂ were studied systematically. In comparison to most existing photodetectors, this self-powered photoelectrochemical photodetector exhibits high-photoresponsivity and fast-response without power supply such as a giant photocurrent density ($\sim$932.8 μA cm^{-2}), an excellent photoresponsivity (4.66 mA W^{-1}), and an ultrafast response/recovery time (3.6/6.4 ms) in the ultraviolet-visible range, which have great potential in various harsh and complex environments. This work provides valuable inspiration for the design of two-dimensional optoelectronic and photoelectrochemical devices with improved performance by the morphology and heterostructure design.

Introduction

Photoelectrochemical (PEC)-type photodetectors have recently received great attention for broad applications in many fields[1–3] due to their simple and low-cost fabrication processes, environmentally friendly nature, high photoresponsivity, and fast response speed. These PEC-type photodetectors can accelerate

Shaanxi Joint Lab of Graphene, Laboratory of Photon-Technology in Western China Energy, International Collaborative Center on Photoelectric Technology and Nano Functional Materials, Institute of Photonics & Photon-Technology, School of Physics, Northwest University, Xi'an 710069, China. E-mail: yxzhou@nwu.edu.cn, xlxuphy@nwu.edu.cn; Tel: +86 029-88303667

† Yuqi Liu and Chunhui Lu contributed equally to this work.

the separation of photoexcited carriers because of the energy barrier at the interface between the photoelectrode material and the electrolyte, and the electrolyte plays the role of an ion channel to finish the whole current loop in the process.[4] Thus, the PEC-type photodetectors have been widely considered as novel self-powered photodetectors even without an external power supply, which have great potential in various harsh and complex environments[5] such as depopulated zones and rescue after disaster. Recently, many traditional semiconductors such as ZnO and TiO₂ have been chosen as photoelectrode materials for self-powered photodetectors, but they can only perform in the ultraviolet region.[6–8] Compared with these traditional electrode materials, two-dimensional (2D) layered semiconductor materials like BP become promising building blocks for self-powered PEC photodetection devices due to their unique physicochemical properties[9] such as broad optical absorption and high carrier mobility. However, these photodetectors need to be further optimized because of irreversible oxidation,[10] low photocurrent density, or low photoresponsivity.[2] Subsequently, with the development of synthesis

methods and nanostructure research, transition metal dichalcogenide (TMD) with excellent optical and electrical properties become a spotlight as key components for the next generation of optoelectronic devices.

Atomic-scale molybdenum disulfide (MoS_2) is the first extensively studied TMD material with high carrier mobility and a broad absorption range from the visible to the mid-infrared region.[11,12] Thanks to these outstanding optical and electrical properties, a MoS_2-based photoconducting photodetector has shown a broadband photoresponse (445–2717 nm) and a maximum responsivity (50.7 mA W^{-1}).[13] However, the photodetection capacity of monolayer MoS_2 is still limited by the low absorption (less than 8% in the visible region)[14] and a relatively long response time (~ 1.5 s),[15] which severely affects the application of self-powered photodetectors. Researchers have tried lots of methods to improve the photoelectric response, including the phase,[16] element doping,[17] defect engineering,[18,19] and heterostructure construction.[20,21] Among these strategies, the formation of van der Waals (vdW) heterostructures is the most promising way because of the rich designability of band alignment.[22,23] Tin dichalcogenide (SnS_2) exhibits a superior absorption coefficient in the ultraviolet-visible (UV-Vis) region,[24,25] a rapid diffusion rate of electron–hole pairs,[26] and large carrier mobility (18–760 cm^2 V^{-1} s^{-1}),[27] and has been viewed as a possible candidate to remedy the shortcomings of MoS_2-based photodetectors. More importantly, SnS_2-based photodetectors have demonstrated a fast response time (~ 5 μs).[28] The vertical bilayer heterostructures of SnS_2/MoS_2 have been reported to have a type-II band alignment, which supports a high photoresponsivity of ~ 1.36 A W^{-1} with a field-effect transistor (FET) structure.[29] Nevertheless, the weak total absorption limited by the inherent ultrathin structure is a common problem for 2D materials in practical applications. Increasing film thickness directly is not a good option because of the structural transition from 2D to bulk. Therefore, constructing SnS_2/MoS_2 heterostructures with special morphology is expected to enhance light absorption. High-density vertically oriented SnS_2 nanosheet arrays[30] and monolayer MoS_2 nanosheets[31] can be obtained by vdW epitaxial growth. Such complementarity in SnS_2 and MoS_2 is expected for designing self-powered PEC photodetectors with outstanding photodetection performances. Moreover, this PEC-type photodetector collects the electrons at the conductive substrate, and then the electrons go into the counter electrode (Pt foil) and are combined with H^+ in the electrolyte, thus producing hydrogen. The reported studies predict in theory that the conduction and valence band edges of SnS_2 and MoS_2 could straddle the electrochemical potentials for water splitting,[32,33] which are also desirable in PEC applications.

In this work, vertically oriented SnS_2 nanosheet arrays with different structural densities are deposited on MoS_2 nanosheets by a two-step vdW epitaxial growth method using a chemical vapor deposition (CVD) technique. A series of characterization studies and PEC measurements have been used to investigate the photodetection properties and physical and chemical mechanisms of the devices. The results confirm that the high density–vertical (HV) SnS_2/MoS_2 heterostructure possesses greatly enhanced self-powered photodetection performances compared with SnS_2, MoS_2, and low density–vertical (LV) SnS_2/MoS_2 heterostructures. Specifically, the photocurrent density and photoresponsivity reach ~ 932.8 μA cm^{-2} and ~ 4.66 mA W^{-1} under zero bias voltage, and the response/recovery time is only $\sim 3.6/6.4$ ms. Additionally, these heterostructures also have relatively good hydrogen evolution reactions. This improvement in photodetection and water splitting comes from the special morphology improving light absorption and the type-II heterostructure accelerating the separation of electron–hole pairs. Our work paves the way for fabricating high-performance self-powered PEC photodetectors by constructing SnS_2/MoS_2 heterostructures with effective structural design, which is also a valuable reference for the design of 2D heterostructures in other potential optoelectronic and PEC applications.

Fabrication of SnS_2/MoS_2

HV-SnS_2/MoS_2 and LV-SnS_2/MoS_2 van der Waals heterostructures were grown by a two-step CVD method (Fig. 1). MoS_2 nanosheets were synthesized on indium tin oxide (ITO) substrates in the first step. As precursors, 3.5 mg MoO_3 (molybdenum oxide, 99.998%, Alfa) and 1 g S (sulfur, $\geq 98\%$, Aladdin) powders were placed in the vacuum tube furnace. The ITO substrates were positioned at the downstream part of the quartz tube, which was purged with a high-purity Ar (argon, 99.9%) gas. Then, the temperatures of zone 1 and zone 2 were ramped up to 200 °C (S) and 680 °C (MoO_3) in 20 minutes, respectively. After maintaining the temperatures for 10 minutes in the Ar atmosphere with a constant flow of 100 sccm, the system was cooled down spontaneously. For the second step, HV-SnS_2 and LV-SnS_2 were prepared on the as-grown MoS_2 nanosheets on ITO glass substrates. For the preparation of HV-SnS_2/MoS_2, 3 mg SnO (Tin oxide, 99.9%, Alfa) and 1 g S powders were chosen as precursors. The temperature zones 1 and 2 were heated to 200 °C (S) and 650 °C (SnO) in 20 minutes,

Fig. 1 Schematic of two-step direct vdW epitaxial growth of low density-vertical (LV) and high density-vertical (HV) SnS_2/MoS_2 heterostructures.

respectively. The growth time is 20 minutes, and the atmosphere is Ar gas with a flow of 30 sccm. To prepare LV-SnS_2/MoS_2, 0.5 g $SnCl_4 \cdot 5H_2O$ (stannic chloride hydrated, 99.0%, Aladdin) and 1 g S powders as precursors were heated to 450 °C and 200 °C in 25 minutes, respectively. The growth temperature is 15 minutes, and the flow rate Ar is 60 sccm. As reference samples, HV-SnS_2 and LV-SnS_2 are also prepared on ITO substrates directly using the heterostructure growth parameters.

Characterization of SnS_2/MoS_2

The optical micrograph of MoS_2 nanosheets on an ITO glass substrate is shown in Fig. 2(a). The randomly deposited island-shaped nanosheets have large areas with diameters of ~10–20 μm and cover almost 70% of the ITO surface. The sectional-view morphology of the HV-SnS_2 sample is characterized by scanning electron microscopy (SEM, Thermo Fisher, Apreo S) in Fig. 2(b). The nanosheets are vertically oriented with a height of ~500 nm. The SnS_2 nanosheets tend to grow out-of-plane on ITO substrate due to the higher surface energy of vertical (100) planes in SnS_2.[34] Similarly, it is found that SnS_2 nanosheets also vertically grow on the ITO with MoS_2 nanosheets, which can be observed from SEM images in Fig. 2(c) and (d). Fig. 2(c) and (d) show the top SEM images of LV-SnS_2/MoS_2 and HV-SnS_2/MoS_2 heterostructure samples, respectively. These SnS_2 nanosheets are well-aligned on MoS_2 nanosheets with an edge length of ~500 nm. Compared with the LV-SnS_2/MoS_2 heterostructure, the HV-SnS_2/MoS_2 sample has a higher density, which provides a much larger exposed surface area of HV-SnS_2 and a better contact interface between HV-SnS_2 and MoS_2 nanosheets.[26] This heterostructure could accelerate the interfacial charge transportation, which is beneficial for the design of high-performance PEC devices.[35,36]

X-ray diffraction (XRD, Bruker, D8 Advance) is used to analyze the crystallographic structure of the samples, as shown in Fig. 3(a). The main diffraction peaks of HV-SnS_2/MoS_2 located at 15.05, 28.29, 3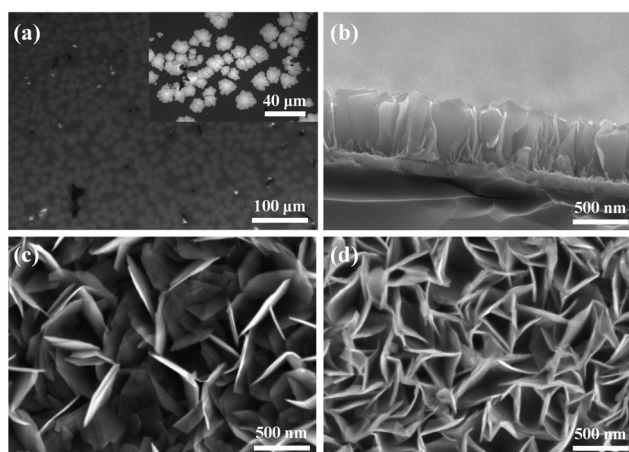0.39, 32.09, 41.79, and 46.23° could be attributed to the (001), (100), (002), (011), (012), and (003) crystal planes from 2H-SnS_2 (JCPDS 89-2358), respectively. The peak at 35.9° comes from the (102) crystal plane of 2H-MoS_2 (JCPDS 37-1492). In the LV-SnS_2/MoS_2 heterostructure, the (001) and (002) crystal planes of SnS_2 and the (102) crystal plane of MoS_2 can be observed. The XRD results demonstrate the coexistence and the good crystallinity of SnS_2 and MoS_2 in the heterostructures.

To further investigate the crystallinity and internal structure of the vdW heterostructure, a transmission electron microscope (TEM, FEI Tecnai G^2 F20) is measured in Fig. 3(b) and (c). The lattice fringes of 0.58 and 0.31 nm can be assigned to the (001) and (100) planes of SnS_2, respectively. The lattice fringe of 0.27 nm corresponds to the (102) plane of MoS_2. In comparison to the TEM image of HV-SnS_2/MoS_2, only the (001) plane of SnS_2 can be observed in LV-SnS_2/MoS_2. This result suggests that HV-SnS_2/MoS_2 might form high density-vertical nanosheets more easily than LV-SnS_2/MoS_2. The TEM characterization reveals the successful formation of the SnS_2/MoS_2 heterostructure.

The linear absorption properties of all samples are analyzed by UV-Vis absorption spectroscopy (R1, Ideaoptics) in Fig. 3(d). The result shows that MoS_2 nanosheets exhibit a broadband absorption from UV to near-infrared light regions, while HV-SnS_2 samples show strong absorption in the UV-Vis region.

Fig. 2 (a) Top optical image of the MoS_2 nanosheets. The inset is a high magnification optical image. (b) Sectional-view SEM image of HV-SnS_2. (c) Top SEM image of LV-SnS_2/MoS_2. (d) Top SEM image of HV-SnS_2/MoS_2.

Fig. 3 (a) XRD pattern of HV-SnS_2/MoS_2, LV-SnS_2/MoS_2, HV-SnS_2, LV-SnS_2, and MoS_2. (b) TEM image of HV-SnS_2/MoS_2. (c) TEM image of LV-SnS_2/MoS_2. (d) UV-Vis absorption spectroscopy of all samples. The inset is Tauc plot for estimating the bandgap energies (E_g) of MoS_2 and HV-SnS_2. (e) Raman spectra of all samples.

The superior absorption property of HV-SnS$_2$ nanosheet arrays is related to their excellent light-trapping structure, which could promote internal light scattering and improve the light-harvesting ability.[25] For the LV-SnS$_2$/MoS$_2$ sample, the absorption is greatly enhanced in the UV-Vis region due to the construction of the heterostructure. Moreover, the increased nanosheet array density induced an even more significant absorption of HV-SnS$_2$/MoS$_2$. The E_g values of MoS$_2$ and HV-SnS$_2$ are 1.88 and 1.93 eV, respectively, obtained from the Tauc plots as shown in the illustration of Fig. 3(d).

Raman spectra of HV-SnS$_2$, LV-SnS$_2$, MoS$_2$, and heterostructure samples are measured by using the SmartRaman confocal-micro-Raman module (developed by the Institute of Semiconductors, Chinese Academy of Sciences). As shown in Fig. 3(e), the characteristic resonance peak at 311.1 cm^{-1} corresponds to the A$_{1g}$ mode of SnS$_2$,[37] and the characteristic resonance peaks at 383.9 cm^{-1} and 402.6 cm^{-1} agree well with the in-plane E$_{2g}$ mode and the out-of-plane A$_{1g}$ mode vibrational modes of MoS$_2$, respectively.[31,38] For both HV-SnS$_2$/MoS$_2$ and LV-SnS$_2$/MoS$_2$ heterostructures, the E$_{2g}$ and A$_{1g}$ peaks of MoS$_2$ and the A$_{1g}$ peaks of SnS$_2$ can be identified. These Raman results demonstrate that the HV-SnS$_2$, LV-SnS$_2$, MoS$_2$, and heterostructure samples are successfully prepared.

X-Ray photoelectron spectroscopy (XPS, Thermo Fisher, ESCALAB Xi+) is applied to analyze the bonding configuration, chemical composition, and electronic structure of the samples. The XPS full spectrum of HV-SnS$_2$/MoS$_2$ heterostructure reveals that Sn, Mo, S, O, and C elements coexist in the sample with a very low content of impurities. Fig. 4(a) shows the binding energy peaks of Sn 3d at $\sim$495.47 and $\sim$497 eV, which are attributed to Sn 3d$_{3/2}$ and Sn 3d$_{5/2}$, respectively, in accordance with the reported values of Sn^{4+}.[39] The Sn 3d$_{5/2}$ peak positions of the HV-SnS$_2$/MoS$_2$ heterostructure and HV-SnS$_2$ have a slight shift of $\sim$0.1 eV, owing to the strong interaction at the HV-SnS$_2$/MoS$_2$ interface in the heterostructure. Fig. 4(b) shows the peaks

of Mo 3d at 232.57 and 229.37 eV, which originate from Mo 3d$_{3/2}$ and Mo 3d$_{5/2}$, respectively.[40] It can be noted that the Mo 3d$_{5/2}$ peak in the HV-SnS$_2$/MoS$_2$ heterostructure is absent, probably because of the shielding of the HV-SnS$_2$ and the heterostructure interaction.

To analyze the carrier transportation properties at the heterostructure interface, high-resolution XPS spectra and the valence band maximum (VBM) are measured in Fig. 4(c). Here, the VBM values of HV-SnS$_2$ and MoS$_2$ are obtained to be 1.93 and 1.05 eV, respectively. The type of HV-SnS$_2$/MoS$_2$ heterostructure can be determined by the valence band offset parameter ΔE_V and the conduction band offset parameter ΔE_C. The ΔE_V for the HV-SnS$_2$/MoS$_2$ heterostructure can be calculated via the method from Kraut et al. as[41]

$$
\Delta E_V = \left(E_{Mo_{3/2}}^{MoS_2} - E_{VBM}^{MoS_2} \right) + \left(E_{Sn_{5/2}}^{SnS_2/MoS_2} - E_{Mo_{5/2}}^{SnS_2/MoS_2} \right) \\ - \left(E_{Sn_{5/2}}^{SnS_2} - E_{VBM}^{SnS_2} \right) \tag{1}
$$

The ΔE_C can be calculated by

$$
\Delta E_C = E_g^{MoS_2} + \Delta E_V - E_g^{SnS_2} \tag{2}
$$

The band alignment information of HV-SnS$_2$/MoS$_2$ is integrated in Fig. 4(d). The results suggest HV-SnS$_2$/MoS$_2$ forms a type-II heterostructure, which could efficiently promote the interfacial charge separation and improve the performance of optoelectronic devices.[42]

Photodetector performance of SnS$_2$/MoS$_2$

The photoelectric responses of the samples are measured by a conventional PEC-type system equipped with an electrochemical workstation (CHI660e, Shanghai Chenhua) and a xenon lamp (PLS-SXE300/300UV, Beijing Perfectlight). A platinum (Pt) wire, a mercurous sulfate electrode, and the prepared samples are used as the counter, reference, and working electrodes, respectively. The electrolyte is 1 mol L^{-1} Na$_2$SO$_4$ neutral solution. The effective illumination area of the photoelectrode is 0.7 cm^2.

To investigate the light power intensity-dependent photoresponse, the amperometric I–t curves without bias voltage are recorded in Fig. 5(a). By tuning the simulated solar power intensity (P) from level I to level VI (P = 200, 150, 100, 75, 50, 20 mW cm^{-2}), the photocurrent shows a downward trend for all the MoS$_2$, HV-SnS$_2$, LV-SnS$_2$, and heterostructure samples. Meanwhile, the photoresponse of the HV-SnS$_2$/MoS$_2$ heterostructure is far more significant than those of LV-SnS$_2$/MoS$_2$, MoS$_2$, HV-SnS$_2$, and LV-SnS$_2$. More specifically, the values of photocurrent density (I_{ph}) can be extracted by

$$
I_{ph} = (I_{light} - I_{dark})/S \tag{3}
$$

where I_{light}, I_{dark}, and S are the current density in the bright state, the current density in the dark state, and the effective illumination area of photoelectrodes, respectively. The calculated I_{ph} values of these samples are shown in Fig. 5(b) on the

Fig. 4 (a) XPS spectra of Sn 3d$_{3/2}$ and Sn 3d$_{5/2}$. (b) XPS spectra of Mo 3d$_{3/2}$ and Mo 3d$_{5/2}$. (c) VB spectra and VBM fitting of HV–SnS$_2$ and MoS$_2$. (d) Band alignment information of HV–SnS$_2$/MoS$_2$.
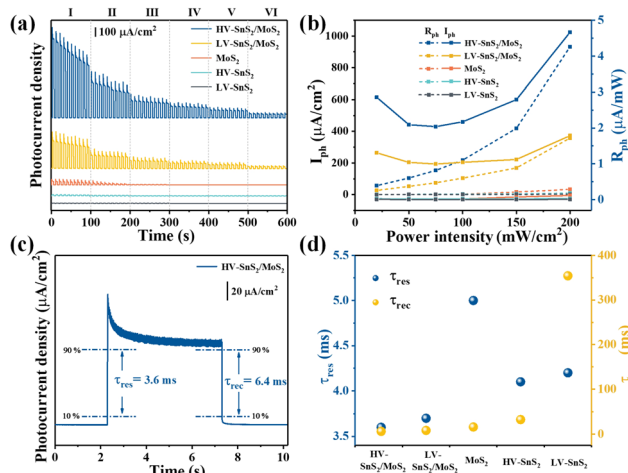
Fig. 5 Photoresponse performances of all samples as photoanodes in 1 M Na_2SO_4 under 0 V. (a) The amperometric $I-t$ curves irradiated by different simulated solar light power intensities (From I to VI: 200, 150, 100, 75, 50, 20 mW cm^{-2}). (b) Photocurrent density (I_{ph}) and photoresponsivity (R_{ph}) as a function of the light power intensity. (c) The time constants of HV-SnS$_2$/MoS$_2$ for the response (t_{res}) and recovery (t_{rec}). (d) The t_{res} and t_{rec} of the samples.

left axis. Taking the optimal HV-SnS$_2$/MoS$_2$ as an example, the value of I_{ph} rises from 57.14 μA cm^{-2} (level VI) to 932.8 μA cm^{-2} (level I) as the light power intensity increases. By comparison, the I_{ph} of HV-SnS$_2$/MoS$_2$ under 200 mW cm^{-2} is 2.6, 27.9, 100.6, and 377.6 times larger than that of LV-SnS$_2$/MoS$_2$, MoS$_2$, HV-SnS$_2$, and LV-SnS$_2$, respectively. The significantly enhanced photoresponse of the heterostructure could be attributed to the fast charge transportation at the interface. Compared with LV-SnS$_2$/MoS$_2$, the better performance of HV-SnS$_2$/MoS$_2$ is related to the improved light absorption due to the high nanosheet array density.

Here, we highlight that the excellent photoresponse of the heterostructure samples is obtained without a bias voltage. This advantage implies a potential self-powered photodetector

application. Therefore, the photoresponsivity parameter (R_{ph}) is introduced to quantitatively evaluate the self-powered photodetection performance, as defined by

$$R_{ph} = I_{ph}/P \qquad (4)$$

The R_{ph} values as a function of P are shown in Fig. 5(b) on the right axis. Under the simulated solar light of 200 mW cm^{-2}, the R_{ph} value of the HV-SnS$_2$/MoS$_2$ heterostructure reaches 4.66 mA W^{-1}, which is 2.6, 39.8, 155.3, and 582.5 times higher than those of LV-SnS$_2$/MoS$_2$, MoS$_2$, HV-SnS$_2$, and LV-SnS$_2$, respectively. Even with a weak light of $\sim$20 mW cm^{-2}, the R_{ph} of the HV-SnS$_2$/MoS$_2$ heterostructure still retains a high value of $\sim$2.85 mA W^{-1}. For comparison, the previously reported R_{ph} values of many 2D and heterostructure materials are summarized in Table 1. These results reveal that the HV-SnS$_2$/MoS$_2$ heterostructure sample has a superior R_{ph}, which is 1000, 28, 71, 2, and 300 times larger than those of BP,[2] PbO,[43] Te@Bi,[44] and BP/MoS$_2$.[45]

In addition to R_{ph}, the response time (t_{res}) and recovery time (t_{rec}) are essential parameters for assessing the response speed of photodetectors. The t_{res} and t_{rec} could be assigned to the time interval of photocurrent density change from 10% to 90% and from 90% to 10% of its peak value, respectively.[43] From Fig. 5(c), the HV-SnS$_2$/MoS$_2$ sample exhibits a remarkably fast response with t_{res} = 3.6 ms and t_{rec} = 6.4 ms as the self-powered PEC photodetector. Additionally, the summarized time constants of HV-SnS$_2$, LV-SnS$_2$, MoS$_2$, and heterostructure samples are shown in Fig. 5(d), and the previously reported results of other 2D materials are listed in Table 1. These results suggest HV-SnS$_2$/MoS$_2$ has a superior response speed compared with BP[2], Te@Bi,[44] SnS,[49] BP/MoS$_2$,[45] SnS$_2$ (FET),[54] and SnS$_2$/MoS$_2$ (FET)[52] based photodetectors. Meanwhile, compared with voltage-driven photodetectors based on MoS$_2$ and SnS$_2$ heterostructures,[34,48,50–53,55,56] the HV-SnS$_2$/MoS$_2$ self-powered photodetector shows a fast response time but relatively lower photocurrent density and responsivity. To improve the

Table 1 Comparison of characteristic parameters of HV-SnS$_2$/MoS$_2$ heterostructure-based photodetector with other reported photodetectors

Materials	Measurement conditions	I_{ph} (μA cm^{-2})	R_{ph} (mA W^{-1})	τ_{res} (ms)	τ_{rec} (ms)	Ref.
HV-SnS$_2$/MoS$_2$	1 M Na$_2$SO$_4$, 0 V	932.8	4.7	3.6	6.4	This work
LV-SnS$_2$/MoS$_2$	1 M Na$_2$SO$_4$, 0 V	357.4	1.8	3.8	8.5	This work
MoS$_2$	1 M Na$_2$SO$_4$, 0 V	33.4	0.1	5	16.3	This work
HV-SnS$_2$	1 M Na$_2$SO$_4$, 0 V	9.3	0.03	4.1	32.8	This work
LV-SnS$_2$	1 M Na$_2$SO$_4$, 0 V	2.47	0.008	4.2	300	This work
BP	0.1 M Na$_2$SO$_4$, 0 V	0.26	0.002	500	500	2
PbO	0.01 M KOH, 0 V	9.8	0.1	—	—	43
Te@Bi	0.5 M KOH, 0 V	4.7	0.03	80	80	44
SnS$_2$/TiO$_2$	0.5 M Na$_2$SO$_4$, 0 V	10	—	—	—	46
BP/MoS$_2$	1 M KOH, 0 V	2.68	0.02	51	—	45
InSe/Ge-doped InSe	1 M KOH, 0 V	0.41	0.003	95	91	47
V-SnS$_2$/gra phene	0.5 M Na$_2$SO$_4$, 0 V	130	—	—	—	48
V-SnS$_2$	0.5 M Na$_2$SO$_4$, 1.4 V	1730	—	—	—	34
SnS	0.1 M Na$_2$SO$_4$, 0.6 V	1.59	0.06	300	—	49
SnS$_2$/Bi$_2$Se$_3$	0.2 M Na$_2$SO$_3$, −0.1 V	170	2.43	—	—	30
TiO$_2$/SnS$_2$/CoO$_x$	0.5 M Na$_2$SO$_4$, 0.65 V	1050	—	—	—	50
V-SnS$_2$	FET, 490 nm V_{ds} = 2 V	0.043	—	43.4	64.4	51
SnS$_2$/MoS$_2$	FET, visible V_{ds} = 1 V	4×10^5	2.3	100	—	52
SnS$_2$/perovskite	FET, 445 nm V_{ds} = −3 V	1050	—	0.02	0.03	53

photodetection capability of HV-SnS$_2$/MoS$_2$, applying an external bias may be an efficient way to accelerate the charge transport process.

To further explore the sensitivity this self-powered photodetector, the wavelength-dependent response is measured. Fig. 6(a) shows the wavelength dependence of the photocurrent density under quasi-monochromatic light irradiation at 350, 380, 420, 450, 475, 500, 520, 550, 600, and 650 nm. The light power intensity maintains a constant of 10 mW cm^{-2}. Moreover, the I_{ph} values are extracted as shown in Fig. 6(b) to give a clear comparison. All these samples show the highest I_{ph} at 420 nm, according well with the absorption spectra in UV-Vis results (Fig. 3(a)). The HV-SnS$_2$/MoS$_2$ heterostructure exhibits the largest I_{ph} under all the measured wavelengths, and the maximum I_{ph} of HV-SnS$_2$/MoS$_2$ at 420 nm reaches $\sim$118.25 µA cm^{-2}, which is 1.9, 9.1, 11.5, and 11.6 times larger than those of LV-SnS$_2$/MoS$_2$, MoS$_2$, HV-SnS$_2$, and LV-SnS$_2$, respectively. The result originates from the special morphology improving light absorption and type-II heterostructure accelerating separation of electron–hole pairs. To make a more general comparison, the R_{ph} values that do not contain the power intensity are calculated and shown in Fig. 6(b) on the right axis. The changing of R_{ph} is proportional to I_{ph} because the P is a constant 10 mW cm^{-2} in the measurement. The HV-SnS$_2$/MoS$_2$ sample also exhibits the highest sensitivity at 420 nm with the maximum R_{ph} of 11.82 mA W^{-1}, which is much more significant than the reported 0.76, 0.54, 0.37, and 0.41 of graphdiyne ($\sim$400 nm),[57] Bi$_2$Te$_3$ ($\sim$400 nm),[58] Bi/Te ($\sim$400 nm),[59] and ZnO/NiO ($\sim$350 nm),[60] respectively. These results suggest that the HV-SnS$_2$/MoS$_2$-based photodetector can be used in the UV-Vis region.

In the following part, we verify the self-powered photoresponse properties of HV-SnS$_2$/MoS$_2$ for visible and infrared detection applications. Different wavelength bands of 400+, 420+, 700+, and 800+ nm are achieved by using cut-off filters.
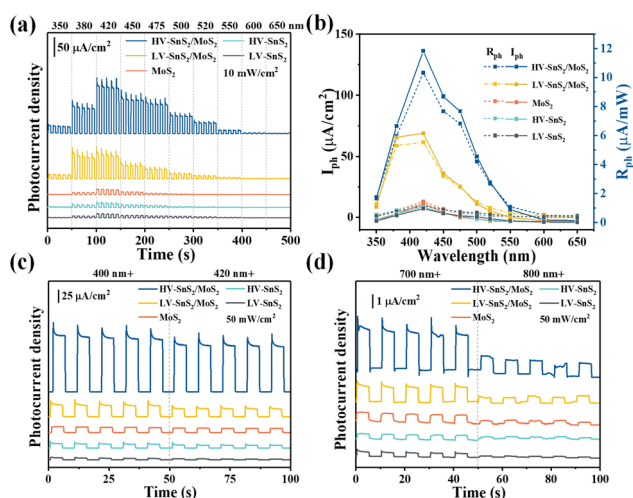
Fig. 6(c) shows the visible light detection performances of the samples under 400+ and 420+ nm irradiation. The HV-SnS$_2$/MoS$_2$ heterostructure offers the best performance, with the photocurrent density reaching 205.9 µA cm^{-2} under 400+ nm irradiation, which is 4.7, 10.3, 13.4, and 36.4 times larger than those of LV-SnS$_2$/MoS$_2$, MoS$_2$, HV-SnS$_2$, and LV-SnS$_2$, respectively. It is worth mentioning that the HV-SnS$_2$/MoS$_2$ heterostructure can also be used as an infrared photodetector. As proved in Fig. 6(d), relatively high photocurrent densities of approximately 2.63 and 0.92 µA cm^{-2} are achieved by HV-SnS$_2$/MoS$_2$ heterostructure under 700+ and 800+ nm irradiation, respectively. The below bandgap absorption may be from the intrinsic defects, such as S vacancies[13] and the surface oxidation.[61]

To understand the charge and mass transfer processes at the photoelectrode/electrolyte interface, electrochemical impedance spectra (EIS) were measured from 10^{-2} to 10^5 Hz, as shown in Fig. 7(a). The inset shows the equivalent circuit consisting of R_s, R_{ct}, and CPE, which represent the electrolyte solution resistance, the charge transfer resistance, and the interfacial capacitance, respectively. The HV-SnS$_2$/MoS$_2$ heterostructure possesses the smallest semicircle radius, suggesting the lowest charge transfer impedance and the highest charge transfer efficiency at the interface between the photoelectrode and the electrolyte. Additionally, the EIS Bode phase plots (Fig. 7(b)) also can reveal the interfacial mass and charge transfer in the low and middle-frequency range (10^{-2} to 10^3 Hz). The frequency (f_{max}) corresponding to the characteristic peak shifts toward lower frequency region after the construction of type-II HV-SnS$_2$/MoS$_2$ heterostructure, suggesting a high-efficiency channel for charge transfer and ion diffusion at the interface between the photoelectrode and the electrolyte.[62]

Fig. 6 (a) The amperometric I–t curves irradiated by light at different wavelengths. (b) I_{ph} and R_{ph} as a function of wavelength. (c) The amperometric I–t curves irradiated by light in 400+ and 420+ nm. (d) The amperometric I–t curves irradiated by light in 700+ and 800+ nm.

Fig. 7 (a) EIS-Nyquist plots of all samples. The illustration is an equivalent circuit model. (b) EIS-Bode phase plots of all samples. (c) Open circuit potential of all samples. (d) Mott–Schottky curves of all samples.

In order to characterize the generation, accumulation, and recombination of electron–hole pairs,[25] the open-circuit potential (V_{oc}) is carried out by monitoring the photoelectrode from a light irradiated quasi-equilibrium state to a dark state. Under light illumination, the photoexcited electrons transfer and accumulate into the conduction band (CB) of the material, leading to a downswing of the Fermi level to a more negative potential.[63] Under the dark state, the V_{oc} decays rapidly because the accumulated electrons will be consumed by holes.[64] As shown in Fig. 7(c), the HV-SnS$_2$/MoS$_2$ has a potential of −0.05 V, which is more negative than those of LV-SnS$_2$/MoS$_2$ (−0.029 V), MoS$_2$ (−0.026 V), HV-SnS$_2$ (−0.017 V), and LV-SnS$_2$ (−0.007 V). These results suggest that the accumulation of photoexcited electrons in the CB from MoS$_2$ to HV-SnS$_2$ could be accelerated by the interfacial separation of electron–hole pairs in the heterostructure.

Mott–Schottky plots of the photoelectrodes are measured in Fig. 7(d). All the samples are n-type semiconductors inferred from the positive slope of the curves.[65] The charge carrier density (N_D) of semiconductors can be calculated using the formula[66]

$$N_D = \frac{2}{e\varepsilon\varepsilon_0}\left(\frac{\mathrm{d}E}{\mathrm{d}\left(\frac{1}{C^2}\right)}\right) \quad (5)$$

where e is the electron charge; ε is the dielectric constant of the semiconductor; ε_0 is the electric permittivity of vacuum; and C is the specific capacity. The parameter $\mathrm{d}E/\mathrm{d}C^{-2}$ can be deduced from the Mott–Schottky curves. As a result, the N_D values of HV-SnS$_2$/MoS$_2$ and LV-SnS$_2$/MoS$_2$ are calculated to be $\sim 3.5 \times 10^{25}$ cm^{-3} and $\sim 2.9 \times 10^{25}$ cm^{-3}, respectively, which are much higher than those of HV-SnS$_2$ ($\sim 1.2 \times 10^{24}$ cm^{-3}), LV-SnS$_2$ ($\sim 0.9 \times 10^{24}$ cm^{-3}), and MoS$_2$ ($\sim 5.9 \times 10^{22}$ cm^{-3}). Additionally, the higher N_D will raise the Fermi level toward their conduction band and then decrease the flat band potential (V_{FB}).[66] The V_{FB} could be extrapolated from the x-intercepts in the Mott–Schottky plots, and the V_{FB} value of HV-SnS$_2$/MoS$_2$ heterostructure is approximately −0.95 V (*vs.* SCE), which is more negative than LV-SnS$_2$/MoS$_2$ (−0.63 V), HV-SnS$_2$ (−0.45 V), LV-SnS$_2$ (−0.44 V), and MoS$_2$ (−0.39 V). These results confirm that the HV-SnS$_2$/MoS$_2$ sample has the most extensive carrier concentration induced by the efficient charge transfer from MoS$_2$ to HV-SnS$_2$ and then to the ITO current collector.[67] Finally, the depletion layer width W of the electrode–electrolyte interface can be estimated using the following formula:[65]

$$W = \sqrt{\frac{2\varepsilon\varepsilon_0}{qN_D}|V - V_{FB}|} \quad (6)$$

where V represents the applied potential. The calculated W of HV-SnS$_2$/MoS$_2$ and LV-SnS$_2$/MoS$_2$ are 2.32 and 2.68 nm, respectively. These values are sufficiently smaller than those of HV-SnS$_2$ (~ 16 nm), LV-SnS$_2$ (~ 19 nm), and MoS$_2$ (~ 98 nm). The small depletion width implies an efficient charge separation in the HV-SnS$_2$/MoS$_2$ sample.
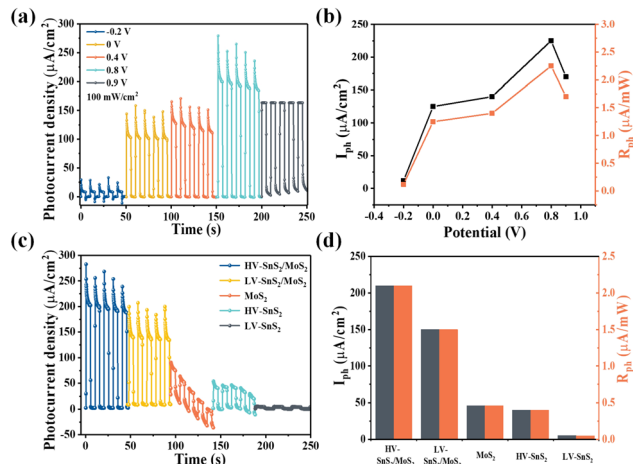

Fig. 8 (a) The amperometric I–t curves of HV-SnS$_2$/MoS$_2$ under different bias voltages. (b) I_{ph} and R_{ph} of HV-SnS$_2$/MoS$_2$ as a function of bias voltage. (c) The amperometric I–t curves of different photoelectrodes under 0.8 V. (d) I_{ph} and R_{ph} of different photoelectrodes under 0.8 V.

Furthermore, we have also investigated the PEC photodetection performances of these samples under non-zero voltages. Previous studies have revealed that the bias voltage is an efficient way to accelerate the charge transport process. The photoresponses of the HV-SnS$_2$/MoS$_2$ sample under different bias voltages are shown in Fig. 8(a). To evaluate the performance of the photodetector, the I_{ph} and R_{ph} values are extracted as shown in Fig. 8(b). Under 0.8 V, the I_{ph} of HV-SnS$_2$/MoS$_2$ reaches a maximum of 213 μA cm^{-2}, which is 25, 1.9, 1.6, and 1.2 times higher than those values measured at −0.2, 0, 0.4, and 0.9 V. Similarly, the values of R_{ph} are proportional to I_{ph} due to the same measured P_λ (100 mW cm^{-2}). The external applied positive voltage could establish a potential gradient within the samples, thus accelerating the charge transport and carrier separation[68] and leading to a better PEC performance. Under the optimal condition of 0.8 V, the photoresponses of HV-SnS$_2$/MoS$_2$, LV-SnS$_2$/MoS$_2$, MoS$_2$, HV-SnS$_2$, and LV-SnS$_2$ are measured in Fig. 8(c), and the calculated I_{ph} and R_{ph} values are shown in Fig. 8(d). This result suggests that the HV-SnS$_2$/MoS$_2$ heterostructure offers more active sites and efficient charge transportation, benefitting PEC water splitting.

Photoelectrocatalytic hydrogen production

The current loop in PEC photodetectors is connected by exchanging electrons with the electrolyte, which may produce hydrogen (H$_2$) and oxygen (O$_2$) evolution at the electrode/electrolyte interface. In order to investigate the PEC water splitting mechanism and photoelectric process, we investigate the PEC water splitting and photoelectrocatalytic H$_2$ evolution of the multifunctional HV-SnS$_2$/MoS$_2$-based PEC photodetector. The photoelectrocatalytic H$_2$ production measurements of these samples are performed in a quartz glass reaction cell equipped with a gas analysis vacuum system (Labsolar-6A, Beijing Perfectlight).

The reaction unit is a conventional three-electrode system under a 100 mW cm^{-2} simulated solar light irradiation (300 W, PLS-SXE300, Beijing Perfectlight). The electrolyte is 100 mL 1 M Na$_2$SO$_4$ aqueous solution without adding any sacrificial reagent. The amount of the generated H$_2$ is analyzed using a gas chromatograph (GC9790II, Fuli instrument).

Fig. 9(a) shows the H$_2$ evolution of the samples and the ITO reference gated at 0.8 V. The ITO has no evident H$_2$ production, indicating that the measured H$_2$ contributes to the electrode. The produced H$_2$ from the HV-SnS$_2$/MoS$_2$ heterostructure reaches 6.8 μmol cm^{-2} within 2.5 h, which is 1.4, 3.4, 3.6, and 5.6 times higher than those from LV-SnS$_2$/MoS$_2$ (4.9 μmol cm^{-2}), MoS$_2$ (2.0 μmol cm^{-2}), HV-SnS$_2$ (1.9 μmol cm^{-2}), and LV-SnS$_2$ (1.2 μmol cm^{-2}). This improvement of H$_2$ production in the HV-SnS$_2$/MoS$_2$ heterostructure might be due to the efficient electron charge transportation at the interface between HV-SnS$_2$ and MoS$_2$ and the low recombination rate of electron–hole pairs. Conversely, the weak photoelectrocatalytic for H$_2$ production of pure LV-SnS$_2$, HV-SnS$_2$, and MoS$_2$ is mainly because of the high recombination rate of the electron–hole pairs.[69] However, the H$_2$ production rate is higher in the first cycle than in the latter, which could be induced by the degraded photo-activity[70] and/or the gradual degradation[71] of the photoanode.

To further explore the contribution of photocatalysis and electrocatalysis, the H$_2$ production of the HV-SnS$_2$/MoS$_2$ heterostructure under 0.8 V without light illumination (electrocatalysis) and under 100 mW cm^{-2} without applied bias potential (photocatalysis) are measured and shown in Fig. 9(b). The electrocatalytic H$_2$ production within 2.5 h is 3.74 μmol cm^{-2}, which is superior to 1.18 μmol cm^{-2} from photocatalytic H$_2$ production. The mechanism of electrocatalytic H$_2$ production can be attributed to the higher applied bias voltage (0.997 V_{NHE}, calculated by $E_{NHE} = E(Ag/AgCl) + 0.197$) than the potential of the cathodic (Pt) H$_2$ evolution reaction.[72] The effect of photocatalytic H$_2$ production is mainly due to the enhanced separation of the photoexcited charge and the more negative CB potential of samples than the H$^+$/H$_2$ potential (0 V_{NHE}).[73] Notably, the photoelectrocatalytic H$_2$ production of HV-SnS$_2$/MoS$_2$ is 6.79 μmol cm^{-2}, which is larger than the total H$_2$ production of photocatalysis and electrocatalysis processes. This result suggests that the synergistic effect of input light activation and applied voltage may accelerate the charge separation and transportation processes.[74]

Based on the above-mentioned results and discussion, the PEC water splitting mechanism of the HV-SnS$_2$/MoS$_2$ heterostructure is investigated in Fig. 9(c). Because the CB potential is approximately 0.3 V lower than the V_{FB} of the n-type semiconductor,[75] the corresponding CB potential of MoS$_2$ and HV-SnS$_2$ are calculated as −0.51 and −0.28 V vs. NHE (vs. the H$^+$/H$_2$ potential of 0.0 V_{NHE}[76,77]), respectively. According to the band alignment of HV-SnS$_2$/MoS$_2$, the energy level arrangement and charge transfer pathways of HV-SnS$_2$/MoS$_2$ are depicted in Fig. 9(c). With simulated light irradiation, the photoexcited electrons are excited from VB to CB in both
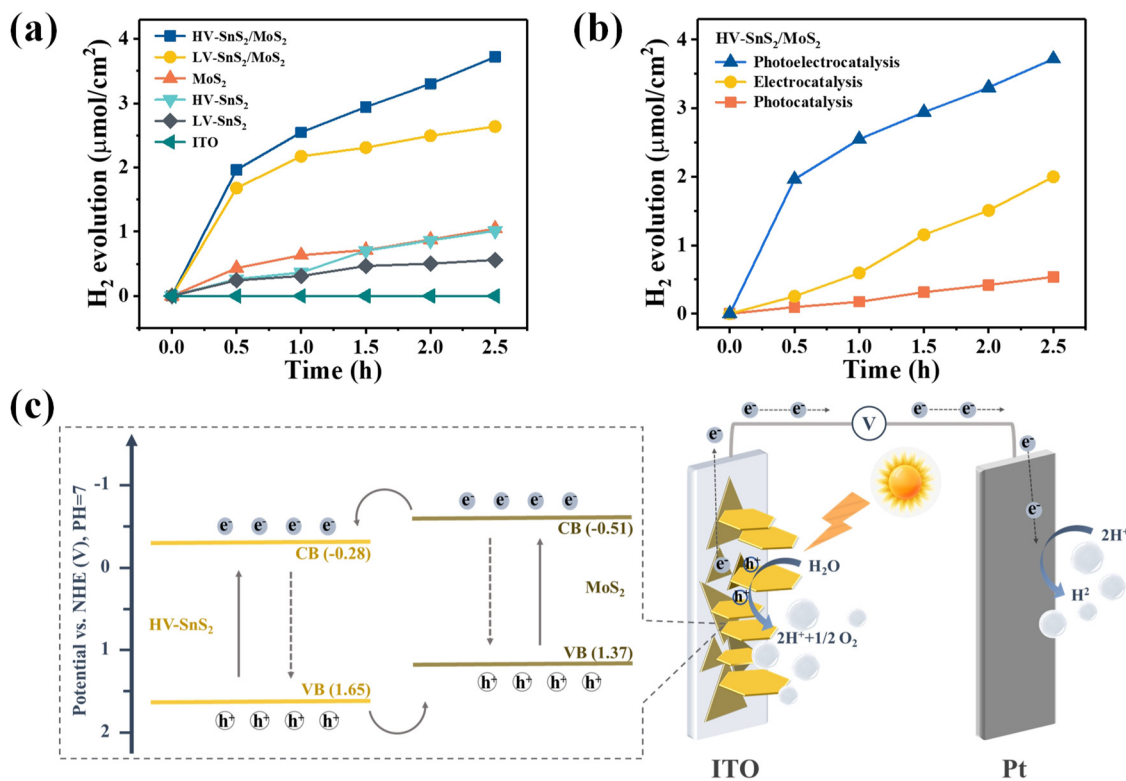
Fig. 9 (a) Photoelectrocatalytic H$_2$ production of different photoanodes in 1 M Na$_2$SO$_4$ under 0.8 V. (b) Photocatalytic (100 mW cm^{-2}), electrocatalytic (0.8 V), and photoelectrocatalytic (100 mW cm^{-2}, 0.8 V) H$_2$ production of HV-SnS$_2$/MoS$_2$ photoanode. (c) The schematic plot of charge transfer pathways in HV-SnS$_2$/MoS$_2$ heterostructure as an effective photoelectrode for PEC water splitting.

MoS_2 and $HV-SnS_2$. At the interface of the $HV-SnS_2/MoS_2$ heterostructure, the electrons transfer from MoS_2 to $HV-SnS_2$ in the CB, then flow to the Pt electrode, and reduce H^+ ions to form H_2 ($2h^+ + 2e^- \rightarrow H_2$). In this process, the charge transfer could be accelerated by the bias voltages, thus boosting the electron transfer to the Pt electrode and improving the H_2 production. In contrast, the hole-transfer pathway is from $HV-SnS_2$ to MoS_2 in the VB. Then, the holes move to the photoelectrode/electrolyte interface and oxidize OH^- ions for producing O_2 ($2H_2O + 2h^+ \rightarrow O_2 + 4e^- + 4H^+$). Therefore, the reverse transmission direction of electrons and holes in $HV-SnS_2/MoS_2$ will efficiently separate electron–hole pairs and decrease their recombination at the heterostructure interface, thus leading to higher H_2 production.

Conclusions

SnS_2/MoS_2 heterostructures with trap-like vertically oriented nanostructures were synthesized through a two-step CVD method. The synthesized $HV-SnS_2/MoS_2$-based PEC photodetector demonstrates excellent self-powered performances, including significantly enhanced photocurrent densities, sensitivity, and stability than those of $HV-SnS_2$, $LV-SnS_2$, MoS_2, and $LV-SnS_2/MoS_2$ heterostructures. The UV-Vis, EIS, V–t, and Mott–Schottky results show that the $HV-SnS_2/MoS_2$ heterostructure has the optimal light absorption range and capacity, the smallest electron transfer impedance, and the highest carrier density. The greatly improved PEC performance of heterostructures could be ascribed to two reasons: (i) the outstanding type-II band alignment at the SnS_2/MoS_2 interface of the heterostructure, which can accelerate the separation and transport of photoexcited charge carriers; (ii) the abundant active sites of high-density vertical SnS_2 on MoS_2 nanosheets, which contribute to more enhanced light absorption. The results could enrich exploration ideas for 2D material-based optoelectronic and PEC applications for photodetection, solar cell, water splitting, and photocatalysis.

Conflicts of interest

There are no conflicts to declare.

Acknowledgements

References

1 J. Zhou, L. Chen, Y. Wang, Y. He, X. Pan and E. Xie, *Nanoscale*, 2016, **8**, 50–73.

2 X. Ren, Z. Li, Z. Huang, D. Sang, H. Qiao, X. Qi, J. Li, J. Zhong and H. Zhang, *Adv. Funct. Mater.*, 2017, **27**, 1606834.

3 X. Ren, W. Zheng, H. Qiao, L. Ren, S. Liu, Z. Huang, X. Qi, Z. Wang, J. Zhong and H. Zhang, *Mater. Today Energy*, 2020, **16**, 100401.

4 H. Qiao, Z. Huang, X. Ren, S. Liu, Y. Zhang, X. Qi and H. Zhang, *Adv. Opt. Mater.*, 2019, **8**, 1900765.

5 L. Peng, L. F. Hu and X. S. Fang, *Adv. Funct. Mater.*, 2014, **24**, 2591–2610.

6 S. M. Hatch, J. Briscoe and S. Dunn, *Adv. Mater.*, 2013, **25**, 867–871.

7 Y. Yang, W. Guo, J. Qi, J. Zhao and Y. Zhang, *Appl. Phys. Lett.*, 2010, **97**, 223113.

8 Y. Xie, L. Wei, G. Wei, Q. Li, D. Wang, Y. Chen, S. Yan, G. Liu, L. Mei and J. Jiao, *Nanoscale Res. Lett.*, 2013, **8**, 188.

9 C. Jin, E. Y. Ma, O. Karni, E. C. Regan, F. Wang and T. F. Heinz, *Nat. Nanotechnol.*, 2018, **13**, 994–1003.

10 J. Zhang, S. Chen, Y. Ma, D. Wang, J. Zhang, Y. Wang, W. Li, Z. Yu, H. Zhang, F. Yin and Z. Li, *J. Mater. Chem. B*, 2018, **6**, 4065–4070.

11 B. Radisavljevic, A. Radenovic, J. Brivio, V. Giacometti and A. Kis, *Nat. Nanotechnol.*, 2011, **6**, 147–150.

12 C. Choi, M. K. Choi, S. Liu, M. S. Kim, O. K. Park, C. Im, J. Kim, X. Qin, G. J. Lee, K. W. Cho, M. Kim, E. Joh, J. Lee, D. Son, S.-H. Kwon, N. L. Jeon, Y. M. Song, N. Lu and D.-H. Kim, *Nat. Commun.*, 2017, **8**, 1664.

13 Y. Xie, B. Zhang, S. Wang, D. Wang, A. Wang, Z. Wang, H. Yu, H. Zhang, Y. Chen, M. Zhao, B. Huang, L. Mei and J. Wang, *Adv. Mater.*, 2017, **29**, 1605972.

14 S. M. Bahauddin, H. Robatjazi and I. Thomann, *ACS Photonics*, 2016, **3**, 853–862.

15 P. Gant, P. Huang, D. Pérez de Lara, D. Guo, R. Frisenda and A. Castellanos-Gomez, *Mater. Today*, 2019, **27**, 8–13.

16 R. Yalavarthi, A. Naldoni, Š. Kment, L. Mascaretti, H. Kmentová, O. Tomanec, P. Schmuki and R. Zbořil, *Catalysts*, 2019, **9**, 204.

17 I. S. Cho, C. H. Lee, Y. Feng, M. Logar, P. M. Rao, L. Cai, D. R. Kim, R. Sinclair and X. Zheng, *Nat. Commun.*, 2013, **4**, 1723.

18 K. Jarasiunas, L. Bastiene, J. C. Launay, P. Delaye and G. Roosen, *Semicond. Sci. Technol.*, 1999, **14**, 48–57.

19 J. Shi, H. n Cui, Z. Liang, X. Lu, Y. Tong, C. Su and H. Liu, *Energy Environ. Sci.*, 2011, **4**, 466–470.

20 Y. Zhang, W. Xu, X. Xu, W. Yang, S. Li, J. Chen and X. Fang, *Nanoscale Horiz.*, 2019, **4**, 452–456.

21 E. Lopriore, E. G. Marin and G. Fiori, *Nanoscale Horiz.*, 2022, **7**, 41–50.

22 Y. Xiao, C. Feng, J. Fu, F. Wang, C. Li, V. F. Kunzelmann, C.-M. Jiang, M. Nakabayashi, N. Shibata, I. D. Sharp, K. Domen and Y. Li, *Nat. Catal.*, 2020, **3**, 932–940.

23 P. Guo, J. Jiang, S. Shen and L. Guo, *Int. J. Hydrogen Energy*, 2013, **38**, 13097–13103.

24 B. Thangaraju and P. Kaliannan, *J. Phys. D: Appl. Phys.*, 2000, **33**, 1054–1059.

25 J. Mu, H. Miao, E. Liu, J. Feng, F. Teng, D. Zhang, Y. Kou, Y. Jin, J. Fan and X. Hu, *Nanoscale*, 2018, **10**, 11881–11893.

26 H. Zhong, G. Yang, H. Song, Q. Liao, H. Cui, P. Shen and C.-X. Wang, *J. Phys. Chem. C*, 2012, **116**, 9319–9326.

27 B. Giri, M. Masroor, T. Yan, K. Kushnir, A. D. Carl, C. Doiron, H. Zhang, Y. Zhao, A. Mcclelland and G. A. J. A. E. M. Tompsett, *Adv. Energy Mater.*, 2019, **9**, 1901236.

28 G. Su, V. G. Hadjiev, P. E. Loya, J. Zhang, S. Lei, S. Maharjan, P. Dong, P. M. Ajayan, J. Lou and H. Peng, *Nano Lett.*, 2015, **15**, 506–513.

29 B. Li, L. Huang, M. Z. Zhong, Y. Li, Y. Wang, J. B. Li and Z. M. Wei, *Adv. Electron. Mater.*, 2016, **2**, 1600298.

30 M. Luo, C. Lu, Y. Liu, T. Han, Y. Ge, Y. Zhou and X. Xu, *Sci. China Mater.*, 2022, **65**, 1000–1011.

31 K. Chen, X. Wan, J. Wen, W. Xie, Z. Kang, X. Zeng, H. Chen and J.-B. Xu, *ACS Nano*, 2015, **9**, 9868–9876.

32 Y. Zhang, Y. Liu, R. Li, M. Saddam Khan, P. Gao, Y. Zhang and Q. Wei, *Sci. Rep.*, 2017, **7**, 4629.

33 D. B. Seo, T. N. Trung, S. S. Bae and E. T. Kim, *Nanomaterials*, 2021, **11**, 1585.

34 G. Liu, Z. Li, T. Hasan, X. Chen, W. Zheng, W. Feng, D. Jia, Y. Zhou and P. Hu, *J. Mater. Chem. A*, 2017, **5**, 1989–1995.

35 X. Tan, X. Wang, L. Zhang, L. Liu, G. Zheng, H. Li and F. Zhou, *Anal. Chem.*, 2019, **91**, 8274–8279.

36 L. Chen, E. Liu, F. Teng, T. Zhang, J. Feng, Y. Kou, Q. Sun, J. Fan, X. Hu and H. Miao, *Appl. Surf. Sci.*, 2019, **467-468**, 698–707.

37 Q. Yang, K. B. Tang, C. R. Wang, D. Y. Zhang and Y. T. Qian, *J. Solid State Chem.*, 2002, **164**, 106–109.

38 H. Li, Q. Zhang, C. C. R. Yap, B. K. Tay, T. H. T. Edwin, A. Olivier and D. Baillargeat, *Adv. Funct. Mater.*, 2012, **22**, 1385–1390.

39 C. Z. Yong, N. D. Zhen, K. W. Li, Z. J. S. Ming and P. Technology, *Sep. Purif. Technol.*, 2011, **81**, 101–107.

40 C. H. Lu, J. Y. Ma, K. Y. Si, X. Xu, C. J. Quan, C. He and X. L. Xu, *Phys. Status Solidi A*, 2019, **216**, 1900544.

41 E. A. Kraut, R. W. Grant, J. R. Waldrop and S. P. J. P. R. L. Kowalczyk, *Phys. Rev. Lett.*, 1980, **44**, 1620–1623.

42 S. Han, Y.-C. Pu, L. Zheng, J. Z. Zhang and X. Fang, *J. Mater. Chem. A*, 2015, **3**, 22627–22635.

43 C. Xing, X. Chen, W. Huang, Y. Song, J. Li, S. Chen, Y. Zhou, B. Dong, D. Fan, X. Zhu and H. Zhang, *ACS Photonics*, 2018, **5**, 5055–5067.

44 Y. Zhang, F. Zhang, L. Wu, Y. Zhang, W. Huang, Y. Tang, L. Hu, P. Huang, X. Zhang and H. Zhang, *Small*, 2019, **15**, e1903233.

45 H. Qiao, Z. Li, Z. Huang, X. Ren, J. Kang, M. Qiu, Y. Liu, X. Qi, J. Zhong and H. Zhang, *Appl. Mater. Today*, 2020, **20**, 100765.

46 L. Sun, Z. Zhao, S. Li, Y. Su, L. Huang, N. Shao, F. Liu, Y. Bu, H. Zhang and Z. Zhang, *ACS Appl. Nano Mater.*, 2019, **2**, 2144–2151.

47 L. Liao, B. Wu, E. Kovalska, F. M. Oliveira, J. Azadmanjiri, V. Mazanek, L. Valdman, L. Spejchalova, C. Xu, P. Levinsky, J. Hejtmanek and Z. Sofer, *Nanoscale*, 2022, **14**, 5412–5424.

48 D.-B. Seo, M.-S. Kim, T. N. Trung and E.-T. Kim, *Electrochim. Acta*, 2020, **364**, 137164.

49 W. Huang, Z. Xie, T. Fan, J. Li, Y. Wang, L. Wu, D. Ma, Z. Li, Y. Ge, Z. N. Huang, X. Dai, Y. Xiang, J. Li, X. Zhu and H. Zhang, *J. Mater. Chem. C*, 2018, **6**, 9582–9593.

50 Z. Cao, Y. Yin, P. Fu, D. Li, Y. Zhou, Y. Deng, Y. Peng, W. Wang, W. Zhou and D. Tang, *Nanoscale Res. Lett.*, 2019, **14**, 342.

51 G. Liu, Z. Li, X. Chen, W. Zheng, W. Feng, M. Dai, D. Jia, Y. Zhou and P. Hu, *Nanoscale*, 2017, **9**, 9167–9174.

52 C. S. R. Kolli, V. Selamneni, B. A. Muñiz Martínez, A. Fest Carreno, D. Emanuel Sanchez, M. Terrones, E. Strupiechonski, A. De Luna Bugallo and P. Sahatiya, *ACS Appl. Mater. Interfaces*, 2022, **14**, 15415–15425.

53 L. Shooshtari, A. Esfandiar, Y. Orooji, M. Samadpour and R. Rahighi, *Sci. Rep.*, 2021, **11**, 19353.

54 Q. Fu, H. Mo, K. Ostrikov, X. Gu, H. Nan and S. Xiao, *CrystEngComm*, 2021, **23**, 2563–2571.

55 D.-B. Seo, T. N. Trung, D.-O. Kim, D. V. Duc, S. Hong, Y. Sohn, J.-R. Jeong and E.-T. Kim, *Nano-Micro Lett.*, 2020, **12**, 172.

56 L. Shooshtari, S. Ghods, R. Mohammadpour, A. Esfandiar and A. Iraji zad, *Sci. Rep.*, 2022, **12**, 7227.

57 Y. Zhang, P. Huang, J. Guo, R. Shi, W. Huang, Z. Shi, L. Wu, F. Zhang, L. Gao, C. Li, X. Zhang, J. Xu and H. Zhang, *Adv. Mater.*, 2020, **32**, e2001082.

58 Y. Zhang, Q. You, W. Huang, L. Hu, J. Ju, Y. Ge and H. Zhang, *Nanoscale Adv.*, 2020, **2**, 1333–1339.

59 Y. Zhang, J. Guo, Y. Xu, W. Huang, C. Li, L. Gao, L. Wu, Z. Shi, C. Ma, Y. Ge, X. Zhang and H. Zhang, *Nanoscale Horiz.*, 2020, **5**, 847–856.

60 C. Wei, J. Xu, S. Shi, R. Cao, J. Chen, H. Dong, X. Zhang, S. Yin and L. Li, *J. Mater. Chem. C*, 2019, **7**, 9369–9379.

61 Y.-R. Chang, P.-H. Ho, C.-Y. Wen, T.-P. Chen, S.-S. Li, J.-Y. Wang, M.-K. Li, C.-A. Tsai, R. Sankar, W.-H. Wang, P.-W. Chiu, F.-C. Chou and C.-W. Chen, *ACS Photonics*, 2017, **4**, 2930–2936.

62 C. J. Liu, Y. H. Yang, W. Z. Li, J. Li, Y. M. Li, Q. L. Shi and Q. Y. Chen, *ACS Appl. Mater. Interfaces*, 2015, **7**, 10763–10770.

63 Y. Yin, E. Liu, H. Li, J. Wan, J. Fan, X. Hu, J. Li, C. Tang and C. J. C. I. Pu, *Ceram. Int.*, 2016, 9387–9395.

64 H. Yang, C. Guo, G. H. Guai, Q. Song, S. P. Jiang and C. M. Li, *ACS Appl. Mater. Interfaces*, 2011, **3**, 1940–1945.

65 Y. Liu, F. Le Formal, F. Boudoire, L. Yao, K. Sivula and N. Guijarro, *J. Mater. Chem. A*, 2019, **7**, 1669–1677.

66 F. Cao, J. Xiong, F. Wu, Q. Liu, Z. Shi, Y. Yu, X. Wang and L. Li, *ACS Appl. Mater. Interfaces*, 2016, **8**, 12239–12245.

67 Q. Liu, H. Lu, Z. Shi, F. Wu, J. Guo, K. Deng and L. Li, *ACS Appl. Mater. Interfaces*, 2014, **6**, 17200–17207.

68 Z. J. Li, H. Qiao, Z. N. Guo, X. H. Ren, Z. Y. Huang, X. Qi, S. C. Dhanabalan, J. S. Ponraj, D. Zhang, J. Q. Li, J. L. Zhao, J. X. Zhong and H. Zhang, *Adv. Funct. Mater.*, 2018, **28**, 1705237.

69 J. Xu and X. Cao, *Chem. Eng. J.*, 2015, **260**, 642–648.

70 J. Kim, W. Yang, Y. Oh, H. Lee, S. Lee, H. Shin, J. Kim and J. Moon, *J. Mater. Chem. A*, 2017, **5**, 2180–2187.

71 F. Jiang, Gunawan, T. Harada, Y. Kuang, T. Minegishi, K. Domen and S. Ikeda, *J. Am. Chem. Soc.*, 2015, **137**, 13691–13697.

72 X. Li, X. Hao, A. Abudula and G. Guan, *J. Mater. Chem. A*, 2016, **4**, 11973–12000.

73 X. Wang, X. Wang, J. Huang, S. Li, A. Meng and Z. Li, *Nat. Commun.*, 2021, **12**, 4112.

74 J. Zhang, X. Zhang and L. Lei, *Sci. Bull.*, 2008, **53**, 1929–1932.

75 W. Yin, L. Bai, Y. Zhu, S. Zhong, L. Zhao, Z. Li and S. Bai, *ACS Appl. Mater. Interfaces*, 2016, **8**, 23133–23142.

76 M. Faraji, M. Yousefi, S. Yousefzadeh, M. Zirak, N. Naseri, T. H. Jeon, W. Choi and A. Z. Moshfegh, *Energy Environ. Sci.*, 2019, **12**, 59–95.

77 R. Sathre, J. B. Greenblatt, K. Walczak, I. D. Sharp, J. C. Stevens, J. W. Ager and F. A. Houle, *Energy Environ. Sci.*, 2016, **9**, 803–819.